

# Structural Characterization of Carbon-Supported Platinum–Ruthenium Nanoparticles from the Molecular Cluster Precursor PtRu<sub>5</sub>C(CO)<sub>16</sub>

Michael S. Nashner, Anatoly I. Frenkel, David L. Adler,<sup>†</sup> John R. Shapley,\* and Ralph G. Nuzzo\*

Contribution from the School of Chemical Sciences and the Frederick Seitz Materials Research Laboratory, University of Illinois, Urbana, Illinois 61801

Received April 1, 1997<sup>⊗</sup>

**Abstract:** We describe the preparation and structural characterization of carbon-supported Pt–Ru nanoparticles with exceptionally narrow size and compositional distributions. The supported bimetallic particles are obtained by reduction of the neutral molecular carbonyl cluster precursor PtRu<sub>5</sub>C(CO)<sub>16</sub> with hydrogen. A detailed structural model of the nanoparticles has been deduced on the basis of studies by in situ extended X-ray absorption fine structure spectroscopy (EXAFS), scanning transmission electron microscopy, microprobe energy-dispersive X-ray analysis, and electron microdiffraction. These experiments show that the bimetallic nanoparticles have a Pt:Ru composition of 1:5 and an average diameter of ca. 1.5 nm and adopt a face-centered cubic closest packing structure. These results demonstrate a marked sensitivity of the metal particle structure to nanoscale size effects inasmuch as the thermodynamically stable phase for bulk alloys of this composition is hexagonal close-packed. The local metal coordination environment, revealed by multiple scattering analysis of the EXAFS data, shows the presence of a nonstatistical distribution of different metal atoms in the nanoparticles. Specifically, Pt shows a marked preference for segregation to the particle surfaces under an ambient H<sub>2</sub> atmosphere. Oxidation of the alloy particle in O<sub>2</sub> produces an outer metal oxide layer surrounding a metal-only core. This oxidation is easily reversed by exposing the nanoparticles to H<sub>2</sub> at room temperature.

## Introduction

Nanometer-sized metal particles continue to attract interest because of their unique physical and chemical properties and the importance of these materials as catalysts.<sup>1–14</sup> The physical properties of nanoparticles, which depend strongly on the perturbations that arise from the large fraction of metal atoms residing at the particle surface, may differ markedly from those characterizing the bulk solid state.<sup>1–7</sup> A significant motivation of current research is the need to develop a predictive

understanding of size effects on the structure and reactivity of supported binary alloy, or bimetallic, nanoscale particles due to the profound improvements they yield in many industrial catalytic processes.<sup>3–5,8,13</sup> Despite the extensive efforts of research to date, such an understanding has yet to be generally realized. This reflects in large part the inherent difficulty of

<sup>†</sup> Current address: KLA Instruments Corp., San Jose, CA.

<sup>⊗</sup> Abstract published in *Advance ACS Abstracts*, July 15, 1997.

- (1) *Clusters and Colloids*; Schmid, G., Ed.; VCH: Weinheim, 1994.  
 (2) Tolles, W. M. In *Nanotechnology: Molecularly Designed Materials*; Chow, G., Gonsalves, K. E., Eds.; ACS Symposium Series 622; American Chemical Society: Washington, DC, 1995; pp 1–18.  
 (3) Sinfelt, J. H. *Bimetallic Catalysts -- Discoveries, Concepts, and Applications*; Wiley: New York, 1983.  
 (4) Gates, B. C.; Guzzi, L.; Knözinger, H. *Metal Clusters in Catalysis*; Elsevier: Amsterdam, 1986.  
 (5) (a) Sinfelt, J. H.; Via, G. H.; Lytle, F. W. *J. Chem. Phys.* **1980**, *72*, 4832. (b) Via, G. H.; Drake, K. F.; Meitzner, G.; Lytle, F. W.; Sinfelt, J. H. *Catal. Lett.* **1990**, *5*, 25. (c) Liang, K. S.; Chien, F. Z.; Hughes, G. J.; Meitzner, G. D.; Sinfelt, J. H. *J. Phys. Chem.* **1991**, *95*, 9974. (d) Davis, R. J.; Boudart, M. *J. Phys. Chem.* **1994**, *98*, 5471. (e) Merlen, E.; Beccat, P.; Bertolini, J. C.; Delichère, P.; Zanier, N.; Didillon, B. *J. Catal.* **1996**, *159*, 178.  
 (6) (a) Malm, J.; Bovin, J.; Petford-Long, A.; Smith, D. J.; Schmid, G. *Angew. Chem., Int. Ed. Engl.* **1988**, *27*, 555. (b) Aleandri, L. E.; Bönemann, H.; Jones, D. J.; Richter, J.; Rozière, J. *J. Mater. Chem.* **1995**, *5*, 749. (c) Bradley, J. S.; Via, G. H.; Bonnevoit, L.; Hill, E. W. *Chem. Mater.* **1996**, *8*, 1895. (d) Rodriguez, A.; Amiens, B.; Chaudret, P.; Casanove, M.-J.; Lacante, P.; Bradley, J. S. *Chem. Mater.* **1996**, *8*, 1978. (e) Kolb, U.; Quaiser, S. A.; Winter, M.; Reetz, M. T. *Chem. Mater.* **1996**, *8*, 1889.  
 (7) Nashner, M. S.; Somerville, D. M.; Lane, P. D.; Adler, D. L.; Shapley, J. R.; Nuzzo, R. G. *J. Am. Chem. Soc.* **1996**, *118*, 12964.  
 (8) (a) Anderson, J. R. *Structure of Metallic Catalysts*; Academic: New York, 1975. (b) Klabunde, K. J.; Li, Y.-X. In *Selectivity in Catalysis*; Davis, M. E., Suib, S. L., Eds.; ACS Symposium Series 517; American Chemical Society: Washington, DC, 1993; pp 88–108.

- (9) (a) Duff, D. G.; Edwards, P. P.; Evans, J.; Gauntlett, J. T.; Jefferson, D. A.; Johnson, B. F. G.; Kirkland, A. I.; Smith, D. J. *Angew. Chem., Int. Ed. Engl.* **1989**, *28*, 590. (b) Tanori, J.; Duxin, N.; Petit, C.; Lisiecki, I.; Veillet, P.; Pileni, M. P. *Colloid Polym. Sci.* **1995**, *273*, 886. (c) Bradley, J. S.; Hill, E. W.; Chaudret, B.; Duteil, A. *Langmuir* **1995**, *11*, 693. (d) Andres, R. P.; Bielefeld, J. D.; Henderson, J. I.; Janes, D. B.; Kolaguta, V. R.; Kubaik, C. P.; Mahoney, W. J.; Osifchin, R. G. *Science* **1996**, *273*, 1690. (e) Whetten, R. L.; Khoury, J. T.; Alvarez, M. M.; Murthy, S.; Vezmar, I.; Wang, Z. L.; Stephens, P. W.; Cleveland, C. L.; Luedtke, W. D.; Landman, U. *Adv. Mater.* **1996**, *8*, 428. (f) Suslick, K. S.; Fang, M.; Hyeon, T. *J. Am. Chem. Soc.* **1996**, *118*, 11960. (g) Sangregorio, C.; Galeotti, M.; Bardi, U.; Baglioni, P. *Langmuir* **1996**, *12*, 5800.  
 (10) (a) Gates, B. C. *Chem. Rev. (Washington, D.C.)* **1995**, *95*, 511 and references therein.

- (11) (a) Chopin, A.; Huang, L.; Theolier, A.; Gallezot, P.; Basset, J. M.; Siriwardane, U.; Shore, S. G.; Mathieu, R. *J. Am. Chem. Soc.* **1986**, *108*, 4224. (b) Shapley, J. R.; Uchiyama, W. S.; Scott, R. A. *J. Phys. Chem.* **1990**, *94*, 1190. (c) Basset, J. M.; Candy, J. P.; Chopin, A.; Nedez, C.; Quignard, F.; Santini, C. C.; Theolier, A. *Mater. Chem. Phys.* **1991**, *29*, 5. (d) Ichikawa, M. *Adv. Catal.* **1992**, *38*, 283. (e) Fung, A. S.; McDevitt, M. R.; Tooley, P. A.; Kelley, M. J.; Koningsberger, D. C.; Gates, B. C. *J. Catal.* **1993**, *140*, 190.  
 (12) (a) Kaminsky, M.; Yoon, K. J.; Geoffroy, G. L.; Vannice, M. A. *J. Catal.* **1985**, *91*, 338. (b) Venter, J.; Kaminsky, M.; Geoffroy, G. L.; Vannice, M. A. *J. Catal.* **1987**, *103*, 450.  
 (13) (a) Iwasita, T.; Nart, F. C.; Vielstich, W. *Ber. Bunsen-Ges. Phys. Chem.* **1990**, *94*, 1030. (b) Leger, J. M.; Lamy, C. *Ber. Bunsen-Ges. Phys. Chem.* **1990**, *94*, 1021. (c) Ross, P. N. *Electrochim. Acta* **1991**, *36*, 2053. (d) Cameron, D. S.; Hards, G. A.; Thomsett, D. In *Proc. Workshop on Direct Methanol-Air Fuel Cells*; Landgrebe, A. R., Sen, R. K., Wheeler, D. J., Eds.; Proceedings Series; The Electrochemical Society: Pennington, NJ, 1992; PV 92–14, pp 10–23.  
 (14) (a) McBreen, J.; Mukerjee, S. *J. Electrochem. Soc.* **1995**, *142*, 3399. (b) Chang, J.-R.; Lee, J.-F.; Lin, S. D.; Lin, A. S. *J. Chem. Phys.* **1995**, *99*, 14798.

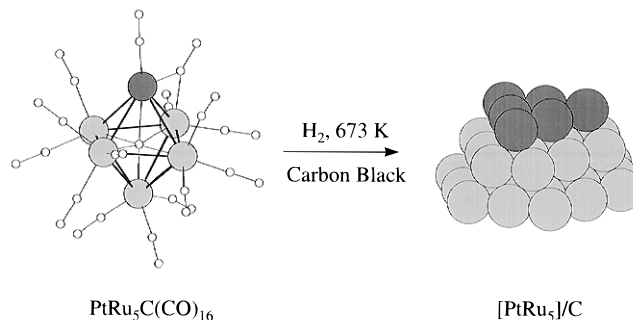
synthesizing supported alloy nanoparticles with narrow distributions of both size and composition as well as the limited availability of methods for their structural characterization.

Multicomponent supported metal catalysts can be prepared by a number of synthetic methods, each with its own distinct advantages. The most commonly used coimpregnation methods involve a support material that has been modified by the adsorption of metal ion precursors from solution.<sup>8,15</sup> The condensation of these centers upon reduction (e.g., in flowing H<sub>2</sub> at high temperature) yields the desired bimetallic particle catalysts. The ability to control the distribution of the particle sizes obtained in this way is quite limited, and the nature of the compositional distributions that characterize the sample is often unknown. An attractive alternative to the coimpregnation method is the use of molecular cluster compounds as precursors.<sup>7,10–12</sup> Molecular clusters may prove advantageous because they precombine the proper stoichiometry of metal atoms as a molecular complex. The hope is that the distributions of size and composition in the particles that result from the activation of these, multimetallic frameworks will be narrower, since their aggregation and growth should be different from that of supported single metal atom precursors. The significant challenge, then, is to devise a molecular cluster precursor that provides a suitable ensemble of metal atoms possessing the necessary heterometallic bonding and stoichiometry. The use of molecular cluster precursors to prepare carbon-supported bimetallic particles has been previously investigated.<sup>12</sup> There have been no reports of the preparation of supported Pt–Ru nanoparticles, materials of interest for applications as electrocatalysts, by using molecular cluster precursors.

Carbon-supported Pt–Ru particles have superior activity as anode catalysts for methanol electrooxidation and demonstrate a marked improvement in resistance to poisoning in comparison to Pt without Ru.<sup>13</sup> These improvements are significant but have not relieved the need for more active electrocatalyst materials for commercially viable direct methanol fuel cells (DMFCs). Much of the current understanding of the mechanisms involved in methanol oxidation with Pt–Ru electrocatalysts is based either on studies of well-defined planar-polycrystalline Pt–Ru electrodes<sup>16</sup> or on the electrochemical polarization responses of model cell assemblies containing fairly significant loadings of the metal alloy catalysts.<sup>13,14</sup> A detailed understanding of the compositional and size dependencies of the electrocatalytic reaction rates over-nanometer-sized supported bimetallic particles remains to be realized.

We report the synthesis and structural characterization of carbon-supported Pt–Ru nanoparticles prepared using the neutral complex PtRu<sub>5</sub>C(CO)<sub>16</sub> as a molecular cluster precursor (see Scheme 1). Our results show that activation of the cluster precursors on the carbon support leads to the formation of bimetallic particles with exceptionally narrow compositional and size distributions. The atomic-scale structure of the resulting particles, referred to hereafter as [PtRu<sub>5</sub>]/C, has been characterized with in situ extended X-ray absorption fine structure

### Scheme 1



(EXAFS) spectroscopy, scanning transmission electron microscopy (STEM), and electron microdiffraction methods. These experiments show that the bimetallic nanoparticles have a Pt:Ru composition of 1:5 and an average diameter of ca. 1.5 nm and adopt a face-centered cubic (fcc) closest packing structure. On the basis of a comparative analysis of the STEM and EXAFS data (which reveal the average nanoparticle size and metal coordination numbers, respectively), the nanoparticles are found to adopt a nonspherical structural motif. The local metal coordination environment, revealed by multiple-scattering analysis of the EXAFS data, shows the presence of a nonstatistical distribution of the different metal atoms in the nanoparticles. Specifically, we find that the Pt atoms in the particle show a pronounced tendency to self-segregate to surface sites on the bimetallic particles. In the presence of O<sub>2</sub>, a surface metal oxide layer is formed with a metal core, but the initial metal-particle structure is recovered unchanged by simply exposing the sample to H<sub>2</sub>.

### Experimental Section

**Sample Preparation.** The molecular cluster precursor, PtRu<sub>5</sub>C(CO)<sub>16</sub>, was prepared by methods described in the literature.<sup>17</sup> A suitable quantity of the compound (1–2 wt % metal loading) was dispersed on carbon black (Vulcan XC-72, Cabot) by incipient wetness from a THF solution. The mixture was allowed to dry in air for 0.5 h.

**Scanning Transmission Electron Microscopy and Electron Microdiffraction.** Microscopy studies were performed using a field emission, Vacuum Generators HB501 STEM operated at 100 kV. The optimal resolution of the microscope is estimated to be ~3 Å. The specimens were prepared by dipping a copper mesh supported holey carbon grid (SPI Supplies) into powdered samples that had been previously activated and examined in situ by EXAFS. Image analysis was performed with Digital-micrograph (Gatan) digital-video data-acquisition software. The particle sizes were determined by measuring the cross-section intensity profiles of individual nanoparticles. The particle diameter was measured as the full width at half-maximum (fwhm) of the intensity profile.

The composition of selected nanoparticles was determined by energy-dispersive X-ray (EDX) analysis.<sup>18,19</sup> In this analysis, the incident electron probe beam was located on a single particle of interest and the X-ray fluorescence from that particle measured. The fluorescence spectra were compared with background spectra measured from a point where no metal was observed. EDX data acquisition and analysis was performed using Link ISIS (Oxford) software, and the quantitative analyses were based on the characteristic X-ray fluorescence lines of Pt and Ru. EDX data were also measured from a standard of known composition, prepared by dispersing the molecular precursor PtRu<sub>5</sub>C(CO)<sub>16</sub> onto a holey carbon Cu grid from a THF solution. The grid was allowed to dry in air and was placed in the microscope for analysis.

(17) Adams, R. D.; Wu, W. *Organometallics* **1993**, *12*, 1248.

(18) Gallezot, P.; Leclercq, C. In *Characterization of Catalysts by Conventional and Analytical Electron Microscopy*; Gallezot, P., Leclercq, C., Eds.; Plenum: New York, 1994; pp 509–558.

(19) Edington, J. W. *Practical Electron Microscopy*; Philips: Eindhoven, The Netherlands, 1975.

(15) Kinoshita, K.; Stonehart, P. In *Preparation and Characterization of Highly Dispersed Electrocatalytic Materials*; Kinoshita, K.; Stonehart, P., Eds.; Plenum: New York, 1977; Vol. 12, pp 183–266. (b) Watanabe, M.; Uchida, M.; Motoo, S. *J. Electroanal. Chem.* **1987**, *229*, 395.

(16) (a) Ross, P. N. In *Proc. Workshop on Direct Methanol-Air Fuel Cells*; Landgrebe, A. R., Sen, R. K., Wheeler, D. J., Eds.; Proceedings Series; The Electrochemical Society: Pennington, NJ, 1992; PV 92–14, pp 51–69. (b) Gasteiger, H. A.; Markovic, N.; Ross, P. N.; Cairns, E. J. *J. Phys. Chem.* **1993**, *97*, 12020. (c) Gasteiger, H. A.; Markovic, N.; Ross, P. N.; Cairns, E. J. *J. Electrochem. Soc.* **1994**, *141*, 1795. (d) Gasteiger, H. A.; Markovic, N.; Ross, P. N.; Cairns, E. J. *J. Phys. Chem.* **1994**, *98*, 617. (e) Gasteiger, H. A.; Markovic, N. M.; Ross, P. N., Jr.; Cairns, E. J. *Electrochim. Acta* **1994**, *39*, 1825. (f) Gasteiger, H. A.; Markovic, N. M.; Ross, P. N. *J. Phys. Chem.* **1995**, *99*, 8290.

Several EDX spectra were measured from the same area to determine if loss of a metal component occurred during analysis.

The long-range microstructure of selected nanoparticles was probed by electron microdiffraction.<sup>19</sup> The probe beam was localized on a nanoparticle of interest, and the diffracted electrons were imaged on a phosphor screen. Nanoparticles located at the edges of the carbon support were chosen for analysis to minimize the diffuse background contributed by the underlying amorphous carbon film or from the carbon black support. The microdiffraction images were acquired using a low-light television camera (RCA) and video taped at 30 frames/s. Representative video images were then digitized (NIH Image). The distances (in pixels) between intensity maxima of the diffraction spots were measured using a cross-section intensity analysis. Typically, the distance between several diffraction spots, arising from lattice planes with the same interplanar spacing, were measured simultaneously. The average spot spacing was determined by dividing as necessary. This procedure was used to minimize systematic errors in the distance measurements. The average spot distances of each reciprocal lattice vector were averaged from several microdiffraction patterns. The distances were converted from pixels to  $\text{\AA}^{-1}$  using the calibration factor determined by measuring spot distances from a reference Si(111) crystal spot pattern.

Theoretical models of hcp (hexagonal close-packed) and fcc  $\text{Pt}_{0.17}\text{Ru}_{0.83}$  alloys were constructed for the purpose of comparing the allowed reflections for the two structures with the microdiffraction data measured from the nanoparticles. The change in the lattice parameter was estimated using Vegard's Law (i.e., a linear variation in the lattice parameter as a function of composition).<sup>20</sup> In the hcp model alloy, the lattice parameters were calculated to be  $a_{\text{PtRu}} = 2.72 \text{ \AA}$  and  $c_{\text{PtRu}} = 4.31 \text{ \AA}$  (based on the actual hcp Ru structure where  $a_{\text{Ru}} = 2.71 \text{ \AA}$  and  $c_{\text{Ru}} = 4.28 \text{ \AA}$  and a model hcp Pt structure where  $a_{\text{Pt}} = 2.80 \text{ \AA}$  and  $c_{\text{Pt}} = 4.44 \text{ \AA}$ ).<sup>21</sup> In the fcc model, a lattice parameter of  $a_{\text{PtRu}} = 3.80 \text{ \AA}$  was used (calculated value based on the actual fcc Pt structure where  $a_{\text{Pt}} = 3.92 \text{ \AA}$  and a model fcc Ru structure where  $a_{\text{Ru}} = 3.79 \text{ \AA}$ ).

**In Situ Extended X-ray Absorption Fine Structure.** To collect in situ X-ray absorption data from the catalyst-containing sample, about 25 mg was pressed at  $\sim 5$  tons into a rectangular wafer (ca.  $1.5 \times 1$  cm) using a hydraulic pellet press. To avoid thickness effects (i.e., self-absorption),<sup>22</sup> pellets were formed with a thickness ( $d$ ) of 0.5 mm satisfying the condition that  $\Delta\mu x \leq 0.1$ , where  $x$  is the effective sample thickness ( $d/\cos 45^\circ$ ) and  $\Delta\mu$  is the absorbance at both the Pt  $L_3$  and Ru K absorption edge steps. The wafer was then loaded into a custom-designed and -built catalyst cell which allowed simultaneous in situ X-ray fluorescence and transmission measurements over an operating temperature range 150–773 K.

The in situ cell was purged with  $\text{H}_2$  for 1 h after loading the sample wafer. The metered flow of  $\text{H}_2$  (Matheson, 99.999%) was passed through sorbent traps (Alltech) to remove  $\text{O}_2$  and water. The temperature was monitored with a chromel/alumel thermocouple (Omega) mounted directly on the sample mounting stage. To activate the samples, each was heated at a rate of 15 K/min in flowing  $\text{H}_2$  (40 mL/min) to a temperature of 673 K and held at that limit for 1 h. The samples were then cooled in the  $\text{H}_2$  atmosphere to 190 K before making the EXAFS measurements.

X-ray absorption data for the Pt  $L_3$  and Ru K edges were also measured from the following reference compounds: Ru powder (Aldrich),  $\text{Pt}_{0.01}\text{Ru}_{0.99}$  alloy, and Pt foil (0.05 mm) (Aldrich). The Ru powder was ground and sieved (200 mesh) to yield an average particle size of less than 10  $\mu\text{m}$ . The  $\text{Pt}_{0.01}\text{Ru}_{0.99}$  alloy was prepared by arc-melting an intimate mixture of the two metals under Ar (20 psi) as described in the literature.<sup>23</sup> The alloy was homogenized at  $\sim 2200^\circ\text{C}$  under an Ar atmosphere for 24 h before being thermally quenched.

All X-ray absorption data were measured at the National Synchrotron Light Source, located at the Brookhaven National Laboratory in Upton, NY. The UIUC/AT&T beamline X16C was used for all measurements.

(20) Wells A. F. *Structural Inorganic Chemistry*, 5th ed.; Oxford: New York, 1984.

(21) Kittel, C. *Introduction to Solid State Physics*, 6th ed.; Wiley: New York, 1986.

(22) Tan, Z.; Budnick, J. I.; Heald, S. M. *Rev. Sci. Instrum.* **1989**, *60*, 1021.

(23) Gasteiger, H. A.; Ross, P. N.; Cairns, E. J. *Surf. Sci.* **1993**, *293*, 67.

The X16C beamline uses a sagittally focusing monochromator with Si(111) crystals which focus 3.5 mrad of light into a  $0.3 \text{ mm} \times 0.5 \text{ mm}$  beam spot at the sample. The intensity of the focused beam ( $I_0$ ) was measured with a 15 in. ion chamber filled with a 10:1 mixture of He:Ar. X-ray absorption data from the sample were measured simultaneously in transmission and fluorescence modes by scanning from 200 eV below to 1000 eV above the Pt  $L_3$  and Ru K edges. This was accomplished by turning the sample to  $\sim 45^\circ$  with respect to the beam direction and measuring the intensity of the transmitted ( $I_t$ ) X-rays and the intensity of the X-ray fluorescence ( $I_f$ ) from the sample. A 15 in. Ar-filled ion chamber placed after the sample (collinear with the beam direction) was used to measure  $I_t$ , and a Lytle detector (the EXAFS Co.) placed at  $90^\circ$  with respect to the beam direction was used to measure  $I_f$ . Thin samples of Pt and Ru metal were used to calibrate the beam energy during each scan of the Pt  $L_3$  and Ru K edges, respectively. The calibration measurement was made with a third ion chamber ( $I_2$ ) placed after  $I_t$ . The positions of the metal absorption edges (Pt, 11 564 eV; Ru, 22 117 eV) could then be determined by placing the metal standard between ion chambers  $I_1$  and  $I_2$  and measuring the total absorption in  $I_2$  due to the metal standard.

**EXAFS Data Analysis.** Analysis of EXAFS data (starting approximately 20–40 eV above the edge energy,  $E_0$ ) has typically depended on availability of phase shifts,  $\delta(k)$ , and backscattering amplitudes,  $f(k)$ , determined experimentally for materials of known crystalline structure.<sup>24</sup> Analysis of the higher-shell data (at distances greater than the first-shell) requires adding the multiple scattering (MS) path contributions which may be comparable to (or larger than) the amplitude of the single scattering (SS) paths. The development of the MS code FEFF (versions 5, 6, and 7)<sup>25</sup> has enabled the analysis of pure materials and alloys to higher  $r$  range.<sup>26,27</sup>

The Pt  $L_3$  and Ru K edge EXAFS data from the nanoparticles were analyzed using the UWXAFS analysis package.<sup>28</sup> Analysis was performed using the following general procedure: (1) the experimental X-ray absorption data from the reference materials and the  $[\text{PtRu}_5]/\text{C}$  nanoparticles were extracted and normalized, (2) model structures of the reference materials were constructed, (3) FEFF6 was used to calculate theoretical photoelectron scattering amplitudes and phase shifts for Pt and Ru absorbing atoms in the model structures, (4) the theoretical EXAFS signal was fit to the experimental EXAFS data, from the reference materials, to determine the most important photoelectron MS paths and to obtain the passive electron amplitude reduction factor,  $S_0^2$ , for the Pt  $L_3$  and Ru K edges,<sup>29</sup> and (5) the EXAFS data from the  $[\text{PtRu}_5]/\text{C}$  nanoparticles were then analyzed by fitting the important scattering paths calculated with FEFF6 to the Pt and Ru edge data, simultaneously.

For each measured X-ray absorption edge, the AUTOBK code<sup>30</sup> was used to normalize and remove the EXAFS,  $\chi(k)$ , from the isolated atom absorption background,  $\mu_0(k)$ , as shown by the following relation:

$$\chi(k) = \frac{\mu(k) - \mu_0(k)}{\Delta\mu_0(0)} \quad (1)$$

In this procedure, the energy reference,  $E_0$ , for the X-ray absorption spectra was chosen at the middle of the edge jump for each spectrum. The photon energy,  $E$ , was then converted into the photoelectron

(24) (a) Koningsberger, D. C.; Prins, R. Eds. *X-ray Absorption: Principles, Applications, Techniques of EXAFS, SEXAFS, and XANES*; Wiley: New York, 1988. (b) Teo, B. K. *EXAFS: Basic Principles and Data Analysis*; Springer-Verlag: New York, 1986.

(25) Zabinski, S. I.; Rehr, J. J.; Ankudinov, A.; Albers, R. C.; Eller, M. *J. Phys. Rev. B* **1995**, *52*, 2995.

(26) (a) Frenkel, A. I.; Stern, E. A.; Qian, M.; Newville, M. *Phys. Rev. B* **1993**, *48*, 12449. (b) Frenkel, A. I.; Stern, E. A.; Voronel, A.; Heald, S. M. *Solid State Commun.* **1996**, *99*, 67.

(27) (a) Frenkel, A. I.; Stern, E. A.; Voronel, A.; Qian, M.; Newville, M. *Phys. Rev. B* **1994**, *49*, 11662. (b) Yacoby, Y.; Stern, E. A. *Ferroelectrics* **1992**, *125*, 263. (c) Rechav, B.; Sicon, N.; Yacoby, Y.; Ravel, B.; Newville, M.; Stern, E. A. *Physica C* **1993**, *209*, 55.

(28) Stern, E. A.; Newville, M.; Ravel, B.; Yacoby, Y.; Haskell, D. *Physica B* **1995**, *208 & 209*, 117.

(29) Stern, E. A.; Heald, S. M. In *Handbook on Synchrotron Radiation*; Koch, E. E., Ed.; North-Holland: Amsterdam, 1983; Vol. 1, Chapter 10.

(30) Newville, M.; Livins, P.; Yacoby, Y.; Rehr, J. J.; Stern, E. A. *Phys. Rev. B* **1993**, *47*, 14126.

wavenumber,  $k$ , using the relation  $k = [2m(E - E_0)/\hbar^2]^{1/2}$ . The edge jump,  $\Delta\mu_0(0)$ , was then determined by the difference in an extrapolated straight line fit to the pre-edge region and the post-edge background absorption function,  $\mu_0(k)$ . The  $\mu_0(k)$  function, which varies smoothly as a function of energy, was approximated by cubic splines. The background function was obtained by minimizing the signal in the low- $r$  region of the Fourier-transformed  $\chi(k)$  data.

The computer code FEFFIT was used to fit theoretical EXAFS calculated with FEFF6 to the experimental  $\chi(k)$  data.<sup>28</sup> In this procedure, FEFF6 was used to calculate the photoelectron scattering-path amplitudes,  $f(k)$ , and phases,  $\delta(k)$ , for the absorbing atom in a model structure. The EXAFS contribution,  $\chi_i(k)$ , from groups of atoms, which lie at approximately the same distance from the absorbing atom (i.e., the  $i$ th shell), was adjusted by applying the EXAFS parameters to  $f_i(k)$  and  $\delta_i(k)$  using the following general relation (for only single scattering paths):

$$\chi_i(k) = \frac{N_i S_0^2}{k R_i^2} f_i(k) e^{-2k^2 \sigma_i^2} \sin(2kR_i + \delta_i(k)) \quad (2)$$

where  $N_i$  is the coordination number (or path degeneracy),  $S_0^2$  is the passive electron amplitude reduction factor,  $R_i$  is the bond distance, and  $\sigma_i^2$  is the EXAFS Debye–Waller factor (DWF).<sup>29</sup> These parameters are varied by FEFFIT until the best least-squares fit is obtained.

To test the reliability of the analysis procedure, the reference data were analyzed first. Experimental EXAFS data from the reference materials were modeled with the corresponding bulk crystal structures. The Pt L<sub>3</sub> data, collected from the Pt foil, were modeled with the fcc crystal structure (where  $a = 3.92$  Å) and the Ru K edge data, collected from the Ru powder, were modeled with the hcp crystal structure (where  $a = 2.71$  Å and  $c = 4.31$  Å).<sup>21</sup> The Pt L<sub>3</sub> data measured from the Pt<sub>0.01</sub>Ru<sub>0.99</sub> alloy were modeled as a single Pt absorbing atom surrounded by a hcp Ru crystal structure. This structure was chosen because, as the phase diagram indicates, the Pt atoms substitute for Ru in the hcp crystal structure at this composition.<sup>31</sup> Furthermore, the dilute composition allows us to assume that the Pt centers form a negligible number of Pt–Pt bonds. After constructing the above models, FEFF6 was used to calculate the amplitude and phase information for each of the possible SS and MS paths that contribute to the  $r$  range of interest.

Because of the limited number of independent points in the experimental EXAFS data, only the dominant MS paths were applied in the fit. Generally, these include the collinear double scattering (DS) and triple scattering (TS) paths<sup>32</sup> and two noncollinear triangular paths<sup>33</sup> which have a large degeneracy in the bulk fcc structure. All of the SS and relevant MS paths were then simultaneously fit to the experimental EXAFS data using the following fitting parameters. The bond distance,  $R_i$ , was varied in each path in accordance with the isotropic lattice expansion (contraction):  $R_i = R_i^{(m)} + \epsilon R_i^{(m)}$  (where  $R_i^{(m)}$  is the model bond distance for path  $i$  and  $\epsilon$  is the isotropic expansion (contraction) factor). The passive electron amplitude reduction factor,  $S_0^2$ , was also varied the same for all paths. The DWFs,  $\sigma_i^2$ , were varied independently for all SS paths while the DWFs of the collinear MS paths were constrained to be equal to that of the fourth-shell SS path.<sup>26</sup>

(31) Okamoto, H. In *Binary Alloy Phase Diagrams*, 2nd ed.; Massalski, T. B., Okamoto, H., Subramanian, P. R., Kacprazate, L., Eds.; ASM: Materials Park, 1990; Vol. 3, p 2345.

(32) The collinear (“focusing”) DS and TS paths, that arise from linear three-atom arrangements, generally contribute a large amplitude to the overall EXAFS function for close-packed structures. For example, in the fcc crystal structure, collinear DS paths result from (1) forward scattering by an atom in the first-shell, and (2) backscattering by an atom in the fourth shell (M–M(1)–M(4)–M). Since this path is time-reversed, there are two times more degenerate scattering paths (i.e., 24) than the number of atoms in the 4th shell of the fcc structure. The collinear TS paths are similar to the DS paths except that the photoelectron scatters from atoms in the first-shell twice (M–M(1)–M(4)–M(1)–M). This path is not time reversed, resulting in only 12 degenerate paths, i.e., the same as the number of atoms in the fourth shell.

(33) Some of the triangle paths may also contribute significantly to the MS amplitude because of their large degeneracy in the fcc structure. These paths arise from noncollinear scattering from two neighbors. For example, two significant triangle paths include scattering between the 1st and 3rd shells, and between two first shells (M–M(3)–M(1)–M and M–M(1)–M(1)–M).

After quantitative determination of the significant MS paths for each model structure and  $S_0^2$  for the Pt L<sub>3</sub> and Ru K edges (0.81(6) and 0.81(4), respectively), the EXAFS data from the [PtRu<sub>5</sub>]/C nanoparticles were fit using an analogous procedure. An fcc crystal structure of Ru, with a lattice parameter of 3.780 Å (giving a  $R_i^{(m)} = 2.673$  Å), was first constructed as a general model of the nanoparticle microstructure. Using this model structure, the theoretical amplitudes and phases of all SS M–Ru( $i$ ) and M–Pt( $i$ ) (where M = Pt and Ru, and  $i$  = backscattering shell) paths from the first to the fourth shell (i.e., an  $r$  range 2–5.5 Å, with M–M(1) = 2.673 Å, M–M(2) = 3.780 Å, M–M(3) = 4.630 Å, and M–M(4) = 5.544 Å) were calculated for each metal absorber, using FEFF6. The calculations were performed with the assumption that the intervening potential (between the absorbing metal and the backscattering shell,  $i$ ) could be approximated with Ru atoms because of the low Pt concentration. Thus, each of the M–Pt( $i$ ) interactions were calculated by substituting Pt backscatterers in only the  $i$ th shell of the Ru crystal structure. The collinear DS and TS paths were also calculated for each metal absorber and fourth-shell backscatterer combination, i.e., M–Ru(1)–M(4). These calculations also used the assumption that Ru atoms were a close approximation of the intervening potential. The approximation that Ru may be used as the only intervening atom was justified because we found that, with Pt as an intervening atom, the change in  $\delta(k)$  was negligible and the change in  $f(k)$  is less than 10%, i.e., within our error bars for coordination numbers.

Each of the relevant scattering paths were fit with FEFFIT to both the Pt and Ru EXAFS data simultaneously using the fitting parameters in the  $\chi_i(k)$  EXAFS equation (eq 2). The passive electron amplitude reduction factor,  $S_0^2$ , was set to the value determined from fitting the reference materials for all paths. The bond distances were varied independently with the constraint that the heterometallic ( $R_{\text{PtRu}(i)}$  and  $R_{\text{RuPt}(i)}$ ) bond distances must be equal in the  $i$ th shell. The heterometallic coordination numbers for shell- $i$  were constrained so that

$$N_{\text{PtRu}(i)} = (X_{\text{Ru}}/X_{\text{Pt}})N_{\text{RuPt}(i)} \quad (3)$$

where  $X_M$  is the atomic percent composition of metal, M, in the nanoparticles ( $X_{\text{Ru}}/X_{\text{Pt}} = 5$ ).<sup>34</sup> The DWFs,  $\sigma_i^2$ , were varied independently for all SS paths with the constraint that the heterometallic disorders were set equal in the  $i$ th shell. The EXAFS parameters ( $N$ ,  $R$ , and  $\sigma^2$ ) which describe the collinear DS and TS paths involving the fourth shell are strictly related to the fourth-shell SS paths in a convex structure.<sup>32</sup> Specifically, the half-pathlengths of the MS paths to the fourth shell (i.e.,  $R_{\text{MM}(DS)}$  and  $R_{\text{MM}(TS)}$ ) must be equal to the distance of the SS path to the fourth shell (i.e.,  $R_{\text{MM}(4)}$ ). The coordination number of the collinear TS paths to the fourth shell must also be equal to the coordination number of the fourth shell (i.e.,  $N_{\text{MM}(4)}$ ). The coordination number of DS paths to the fourth shell was two times larger than the fourth-shell coordination, due to time reversibility of this path.

The FEFFIT code was applied using a two-step procedure where the Pt and Ru data sets were analyzed simultaneously. First, the data range 2.0–3.1 Å was fit with the first-shell SS paths (i.e.,  $\chi(k)_{\text{PtPt}(1)}$ ,  $\chi(k)_{\text{PtRu}(1)}$ ,  $\chi(k)_{\text{RuPt}(1)}$ , and  $\chi(k)_{\text{RuRu}(1)}$ ). Then, the first-shell fit results were fixed and the higher-shell SS and MS paths were varied in the  $r$  range 3.1–5.5 Å. This procedure was justified due to the large separation between the first shell and the second through fourth shells and their substantially different amplitudes.

## Results

Supported bimetallic nanoparticles were prepared by heating the carbon-supported PtRu<sub>5</sub>C(CO)<sub>16</sub> compound to 673 K in an H<sub>2</sub> atmosphere. The structure of these particles on an atomic scale was deduced by using several independent methods.

**Characterization of Nanoparticle Structure and Composition by Scanning Transmission Electron Microscopy.** Representative bright and dark field images of the carbon-supported [PtRu<sub>5</sub>]/C nanoparticles are shown in Figure 1. The samples

(34) Via, G. H.; Drake, K. F.; Meitzner, G.; Lytle, F. W.; Sinfelt, J. H. *Catal. Lett.* **1990**, *5*, 25.

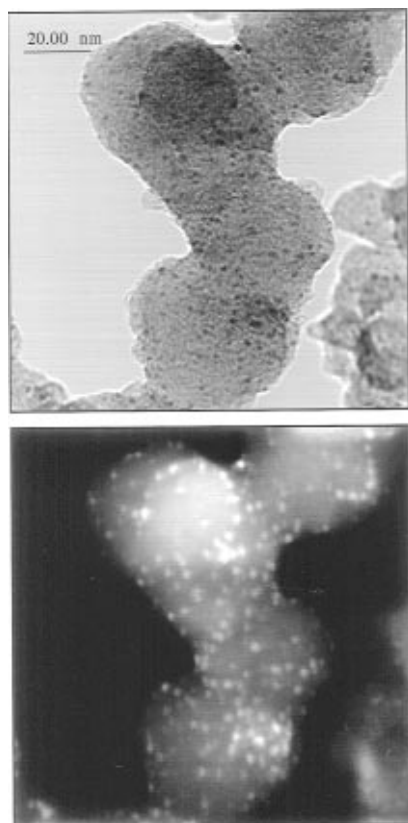


**Figure 1.** Representative STEM bright (upper) and dark field (lower) images ( $\times 10^6$ , 100 kV) of the carbon-supported [PtRu<sub>5</sub>]/C nanoparticles.

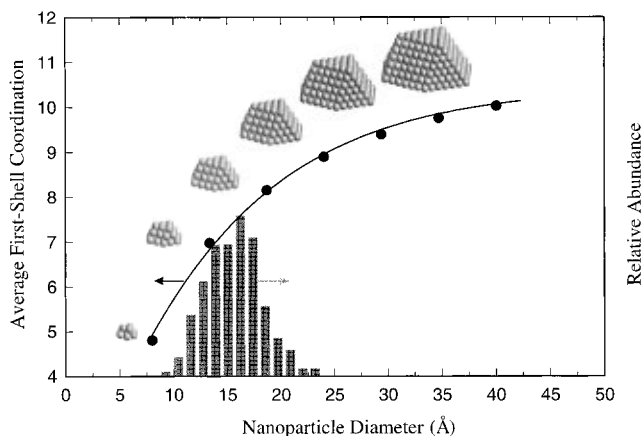


**Figure 2.** Histogram of the particle size distribution (right axis) of the [PtRu<sub>5</sub>]/C nanoparticles measured from multiple STEM images taken in different sample regions. The scale on the left axis shows the correlation between the average first-shell coordination number and diameter for model hemispherical fcc nanoparticles with an edge length of two to eight atoms.

analyzed in the micrographs are the same ones prepared and characterized in the in situ EXAFS experiment. As indicated in the particle size histogram (Figure 2), the metal particles have an average diameter of 1.6 nm and, most significantly, evidence a very narrow size distribution. The sizes of the particles seen in these images suggest that the typical particle is obtained from a reductive condensation of ca. 10 PtRu<sub>5</sub>C(CO)<sub>16</sub> units (see below).

The compositions of individual nanoparticles were determined by atom probe energy-dispersive X-ray analysis (EDX).<sup>18,19</sup> Representative EDX spectra measured with a 10 Å (100 kV) beam incident on a single nanoparticle and a region of the support, immediately adjacent to it are displayed in Figure 3;

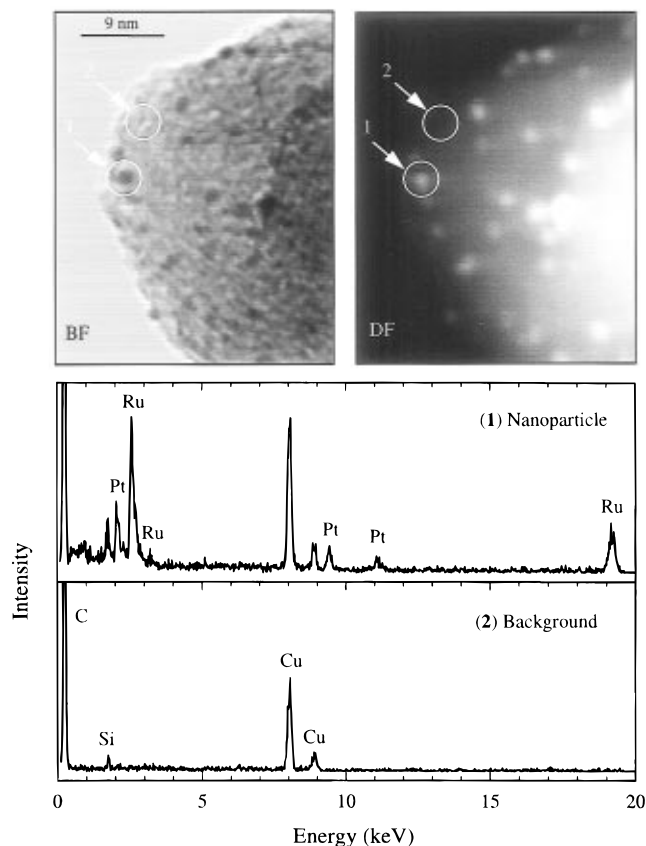


**Figure 3.** Representative EDX spectra measured by locating the electron beam ( $\sim 10$  Å) on a [PtRu<sub>5</sub>]/C nanoparticle (spectrum 1) and on a region of the carbon-support where no metal was observed (spectrum 2). The beam locations are illustrated in the bright and dark field STEM images shown above the spectra. The measured X-ray fluorescent lines include the following: C K $\alpha$ , 0.2 keV; Si K $\alpha$ , $\beta$ , 1.8 keV; Cu L $\alpha$ , $\beta$ , 0.9 keV; Cu K $\alpha$ , 8.0 keV; Cu K $\beta$ , 8.9 keV; Ru L $\alpha$ , $\beta$ , 2.6 keV; Ru L $\gamma$ , 3.2 keV; Ru K $\alpha$ , 19.2 keV; Pt M $\alpha$ , $\beta$ , 2.1 keV; Pt L $\alpha$ , 9.4 keV; Pt L $\alpha$ , 11.1 keV; and Pt L $\beta$ , 11.3 keV. The presence of Cu and Si fluorescence is due to scattering from the supporting grid.

Cu fluorescence is due to diffuse scattering from the supporting grid. Quantitative analysis of the fluorescence yield (Figure 3, spectrum 1) reveals a composition of 16 atom % Pt and 84 atom % Ru in the irradiated nanoparticle. The average of measurements made on 140 particles from different sample regions was  $86 \pm 3$  atom % (Figure 4). The composition of these particles is indistinguishable from that measured from the reference sample of the molecular precursor, PtRu<sub>5</sub>C(CO)<sub>16</sub>, which had an average measured Ru content of  $86 \pm 1$  atom %. These latter values compare well with those expected on the basis of the known stoichiometry of the complex (the few percent deviation is well within the error limits of the detector calibration).

The nanoparticle microstructure was further studied by electron microdiffraction using the STEM. The high quality of the electron optics of the STEM offers the ability to focus the electron beam with sufficient intensity to measure any resulting diffraction from the ordered habits present in nanometer-sized particles.<sup>19</sup> Strong diffraction patterns are seen for these particles as is shown by the representative data presented in Figure 5. The spot patterns measured correspond to an image taken normal to the incident beam direction of a planar section through the reciprocal lattice. Figure 5a,c shows two representative diffraction patterns measured promptly ( $< 2$  s) after illumination of two separate nanoparticles (continuous electron illumination of the particles leads to the degradation of the

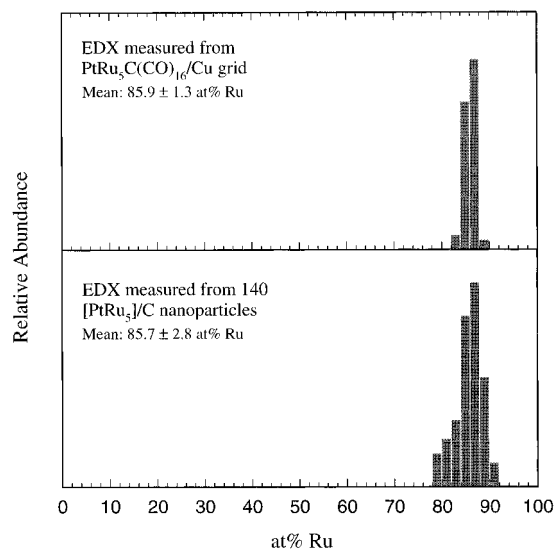


**Figure 4.** Comparison between the atomic fraction of Pt and Ru determined by quantitatively analyzing the EDX spectra measured from the reference  $\text{PtRu}_5\text{C}(\text{CO})_{16}$  cluster (top) and from 140  $[\text{PtRu}_5]/\text{C}$  nanoparticles (bottom).

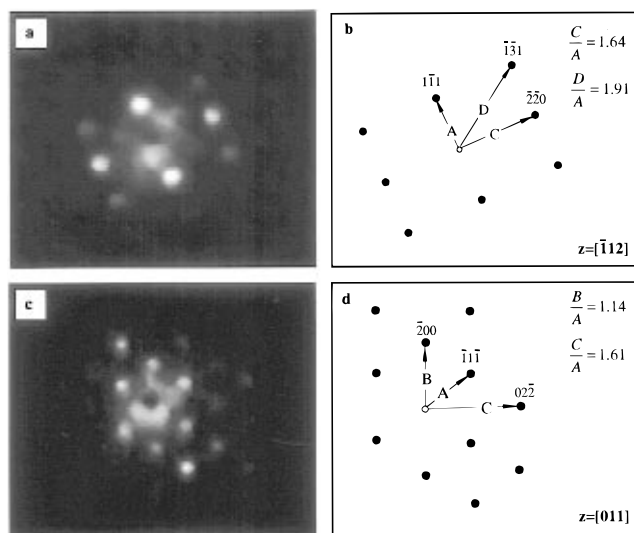


**Figure 5.** Representative microdiffraction images measured from a 1.5 and 1.8 nm (a and c, respectively) particle found in different regions of the  $[\text{PtRu}_5]/\text{C}$  sample. The diffraction patterns a and c were indexed to an fcc structure as shown in b and d, respectively. The ratios of the indicated vectors (A–D) measured from the diffraction images are also shown.

diffraction patterns<sup>35,36</sup>). The patterns shown in the figure (and others recorded at several locations of the sample) are best indexed to a fcc structure with zone axes as shown in Figure 5b,d (see below).<sup>19</sup> On the basis of this assumption, we also have included in the figure the ratios of the distances between several of the identifiable planes:  $\{111\}$  (A),  $\{200\}$  (B),  $\{022\}$  (C), and  $\{131\}$  (D).

To justify the assignment of the microdiffraction patterns (Figure 5a,c) to a close-packed structure, model hcp and fcc  $\text{Pt}_{0.17}\text{Ru}_{0.83}$  alloys were constructed for the purpose of comparing the allowed diffraction planes with the experimentally measured

(35) The degradation of the diffraction pattern is not understood. It may result from the “melting” of the cluster surface under the intense electron beam or, alternatively, be related to a contamination effect due to beam induced deposition of carbon from the background gases.

(36) Vanfleet, R. R.; Mochel, J. M. In *Proceedings of the Microstructure Evolution During Irradiation*; Diaz de la Rubia, T., Was, G. S., Robertson, L. W., Hobbs, L. W., Eds.; Materials Research Society, Pittsburgh, PA, in press.

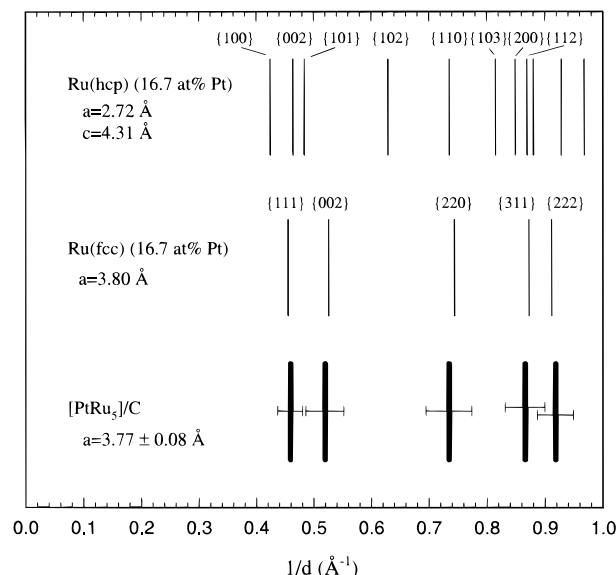


**Figure 6.** Calculated  $1/d$  spacing for diffracting planes in a model  $\text{Pt}_{0.17}\text{Ru}_{0.83}$  alloy with an hcp crystal structure (upper) and an fcc crystal structure (middle) are compared with the values measured by microdiffraction from the  $[\text{PtRu}_5]/\text{C}$  nanoparticles (lower). Error bars were estimated by propagating the deviations ( $1\sigma$ ) from measurements of the Si(111) standard (instrumental) and the nanoparticles.

data (as described in the Experimental Section). The values of the ratios of distances calculated for the fcc Pt–Ru alloy (where  $a_{\text{PtRu}} = 3.80 \text{ \AA}$ ,  $B/A = 1.155$ ,  $C/A = 1.633$ , and  $D/A = 1.915$ ) agree closely with those measured from the microdiffraction patterns. Further confirmation of the preferred formation of fcc nanoparticles was obtained by averaging the distances measured from the diffraction patterns of a variety of nanoparticles residing in different regions of the sample. These averaged values were then converted from pixels to  $1/(d \text{ spacing}) (\text{\AA}^{-1})$ , using a Si(111) reference sample. These values are plotted in Figure 6. For comparison, Figure 6 also includes the allowed Bragg peaks found in a Pt–Ru alloy which adopts either an hcp or fcc structure.<sup>37</sup> As is immediately evident, the ratios of the  $d$  spacing for the reflections measured experimentally correlate best with the fcc crystal structure. The calculated average lattice parameter of  $3.77 \pm 0.08 \text{ \AA}$  also agrees with the nearest-neighbor (NN) bond distances determined from EXAFS data.

**Structure Deduced from the Measurement of *in-situ* EXAFS.** Figure 7 displays the background subtracted  $k^2$ -weighted Pt  $L_3$  edge spectra collected from Pt foil and the  $\text{Pt}_{0.01}\text{Ru}_{0.99}$  alloy, and the Ru K-edge spectrum from Ru powder. The Pt  $L_3$  and Ru K edge EXAFS data collected from the  $[\text{PtRu}_5]/\text{C}$  nanoparticles are presented in Figure 8. The similarity between the functional form of EXAFS amplitudes measured from the reference materials and the  $[\text{PtRu}_5]/\text{C}$  nanoparticles suggests that the Pt and Ru centers are coordinated by predominantly metal scatterers in the nanoparticles.<sup>24,29</sup> The significant reduction in the scattering amplitude (Figure 8) seen over the entire  $k$  range, in comparison to the reference amplitudes (Figure 7), is directly reflective of a lower average coordination number. Figures 9 and 10 display the magnitude of the Fourier-transformed (FT) EXAFS data which yield the non-phase-corrected EXAFS radial structure functions around the Pt and Ru centers. As we show below, the dominant peak at ca.  $2.5 \text{ \AA}$  in the FT data (Figure 10) obtained from the supported nanoparticles results from a combination of scattering

(37) Cullity, B. D. *Elements of X-ray Diffraction*; Addison-Wesley: Reading, MA, 1978.

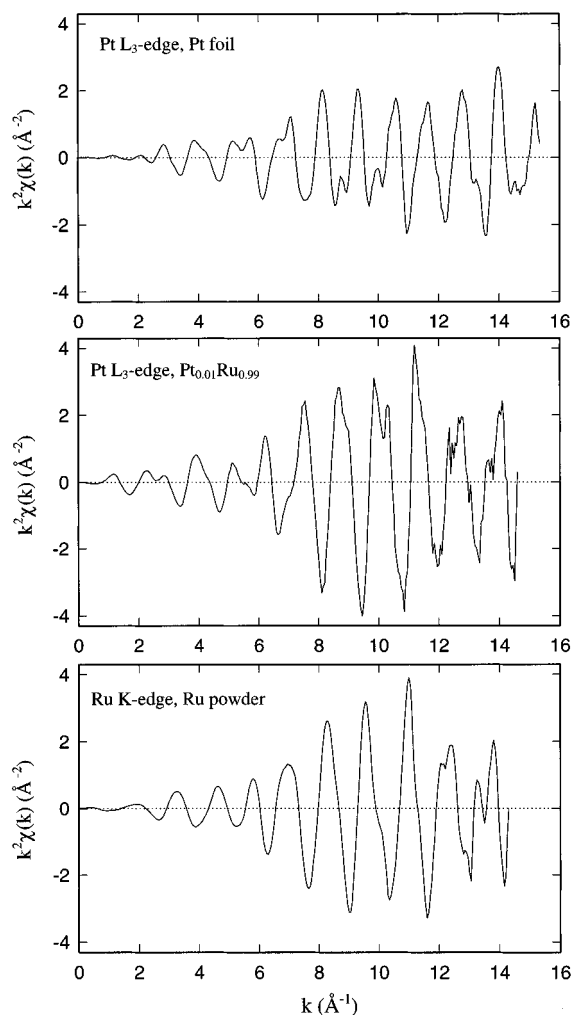


**Figure 7.** Raw  $k^2\chi(k)$  ( $\text{\AA}^{-2}$ ) EXAFS data measured from the reference materials at 190 K: (a) the Pt  $L_3$  edge from a Pt foil (0.05 mm); (b) the Pt  $L_3$  edge from a Pt<sub>0.01</sub>Ru<sub>0.99</sub> alloy; (c) the Ru K edge from Ru powder ( $<10 \mu\text{m}$ ).

from Pt and Ru atoms in the first shell (i.e., nearest neighbors). Both data sets from the nanoparticles also show a significant higher-shell coordination (i.e., in the  $r$  range 3–5.6  $\text{\AA}$ ) that is similar in form to the structure exhibited by the reference EXAFS data. The Pt edge data, however, have distinctively larger signals in the higher shells than the Ru edge data. This must be related to a nonstochastic distribution of metal atoms in the nanoparticles. We will quantify these structural features using theoretical data calculated with FEFF6 for an fcc structural model.

The apparent nonstatistical environments of the Pt and Ru atoms, described above, could only be quantified by fitting the first- and higher-shell EXAFS data. The EXAFS signal in this  $r$  range (3–5.6  $\text{\AA}$ ) consists of at least four SS paths in close-packed structures. A large number of unique MS paths (12 and 26 for fcc and hcp, respectively) also contribute to the EXAFS signal in this  $r$  range, complicating the analysis. Fortunately, as we describe below, the higher-shell analysis was simplified because, in the close-packed structures, a small number of MS paths contribute the largest amplitude (i.e., the collinear DS and TS paths), allowing the other paths to be neglected.<sup>38</sup> We tested this hypothesis using theoretical EXAFS data to fit the structurally well-defined reference materials (i.e., bulk Pt, Ru, and Pt<sub>0.01</sub>Ru<sub>0.99</sub>) to find which paths made significant contributions to the higher-shell EXAFS data. This

(38) Lee, P. A.; Pendry, J. B. *Phys. Rev. B* **1975**, *11*, 2795.

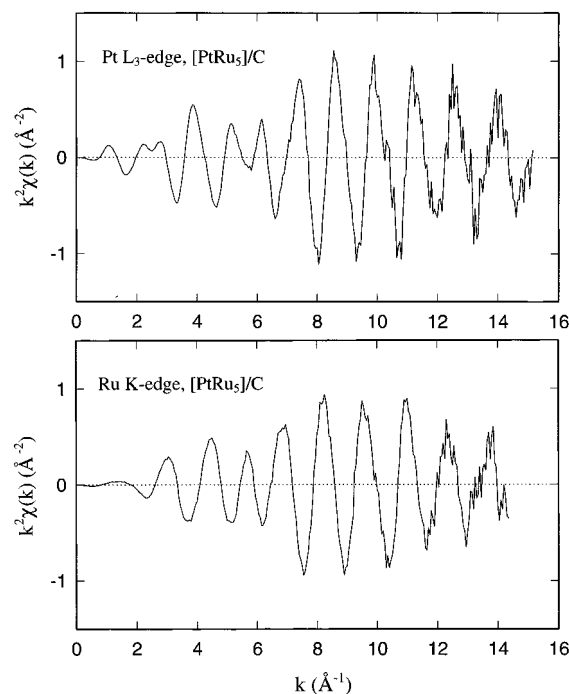


**Figure 8.** Raw  $k^2\chi(k)$  ( $\text{\AA}^{-2}$ ) EXAFS data measured at 190 K from carbon-supported [PtRu<sub>5</sub>]/C nanoparticles after activation at 673 K under H<sub>2</sub> (1 atm): (a) Pt  $L_3$  and (b) Ru K edges.

procedure was also necessary to independently determine the passive electron amplitude reduction factor ( $S_0^2$ ) for the Pt and Ru absorbing atoms because of its strong correlation (see eq 2) with the coordination number and Debye–Waller factor ( $\sigma^2$ ).

The first- and higher-shell Pt foil EXAFS was analyzed by fitting, over the  $r$  range 2–6.5  $\text{\AA}$ , with an fcc structural model. The experimental EXAFS data (35 independent points) and the  $r$  space fit are displayed in Figure 9. The best fit with a minimum number of variables (10) was obtained when the fit included the SS paths from the central atom to the fifth shell ( $R_{\text{Pt}(5)} = 6.20 \text{\AA}$ ) and the two collinear focusing DS and TS paths.<sup>32</sup> The first-shell bond distance ( $2.768 \pm 0.003 \text{\AA}$ ) calculated from the fit was in excellent agreement with the actual value ( $2.772 \text{\AA}$ ). The  $S_0^2$  factor was found to be ( $0.81 \pm 0.06$ ) within the physically expected value (0.7–1.0). As a further test of the first-shell fit quality for  $S_0^2$  and the DWF, which are highly correlating fitting variables, the latter was independently calculated with an Einstein model<sup>39</sup> using the known value of the Pt Debye temperature, 225 K.<sup>40</sup> Using the Einstein model, we obtained a DWF ( $\sigma^2 = 0.0029 \text{\AA}^2$ ) that was in excellent agreement with our previous fit result. The agreement with these two approaches characterizes the high quality of fit to the theoretical data for the reference material and demonstrates the precision with which FEFF6 can be employed to calculate the theoretical scattering interactions. It also demonstrates that, in the fcc crystal structure, the MS contribution to the experimental EXAFS can be approximated satisfactorily with the dominant collinear DS and TS paths (including the triangular paths did not significantly improve the fit results).

The Ru metal and alloy data were fit with the hcp model using a procedure similar to the Pt metal reference fit. In the hcp model structure, only the SS paths within the  $r$  range 2–4.4  $\text{\AA}$  were used. The experimental EXAFS (20 independent points) and fit results for six variables are displayed in Figure 9. The first-shell bond distance ( $2.657 \pm 0.004 \text{\AA}$ ) and  $S_0^2$  ( $0.81 \pm 0.04$ ) are also consistent with the physical model ( $2.651 \text{\AA}$ ).

(39) Frenkel, A. I.; Rehr, J. J. *Phys. Rev. B* **1993**, *48*, 585.

(40) Sandstrom, D. R. *Phys. Rev. B* **1985**, *32*, 3541.

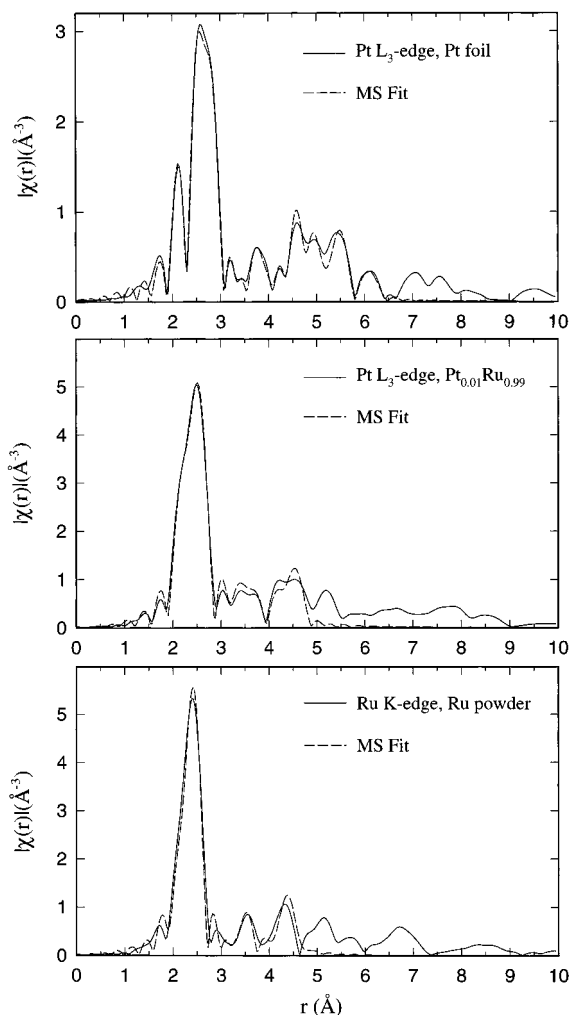


**Figure 9.** Fourier-transformed EXAFS data measured from the reference materials at 190 K (solid) and the multiple scattering fit results (dash): (a) Pt  $L_3$  edge from a Pt foil (0.05 mm); (b) Pt  $L_3$  edge from the  $Pt_{0.01}Ru_{0.99}$  alloy; (c) Ru K edge from Ru powder ( $<10 \mu\text{m}$ ).

Figure 9 also shows the fit (5 variables) to the Pt  $L_3$  data ( $r$  range = 2–4.4 Å, 21 independent points) measured from the  $Pt_{0.01}Ru_{0.99}$  alloy. In the fit, the value of  $S_0^2$  was fixed at the value found in the Pt metal (0.81). Using the hcp model, a fit was obtained that indicated a bond distance of  $2.702 \pm 0.003$  Å (first shell: six NN at 2.672(3) Å, second shell: six NN at 2.731(3) Å). The first-shell distance is about 0.02 Å longer than the value found in Ru metal and 0.07 Å shorter than the value found in Pt metal, a result consistent with a local expansion of the Ru host lattice by the larger Pt atoms.

Fitting the nanoparticle data was performed to first verify the presence of a close-packed shell structure and then to extract the structural parameters for each metal absorber. Both back-scatterers (Pt and Ru) had to be accounted for in the fits of the Pt and Ru EXAFS data. Therefore, all possible single and multiple scattering Pt–M( $i$ ) and Ru–M( $i$ ) paths (where M = Pt and Ru) from the  $i$ th shell had to be accounted for in the theoretical EXAFS that was fit to the Pt  $L_3$  and Ru K edges, respectively. Several simplifying assumptions (as described in the Experimental Section) were made to constrain the large number of variables. Briefly, the nanoparticle structure was modeled with the fcc structure, the number of heterometallic bonding interactions was fixed in accordance with the 1:5 composition, and the MS interactions were approximated by only using the collinear DS and TS paths that were found to be important in the fits to the reference Pt foil data.

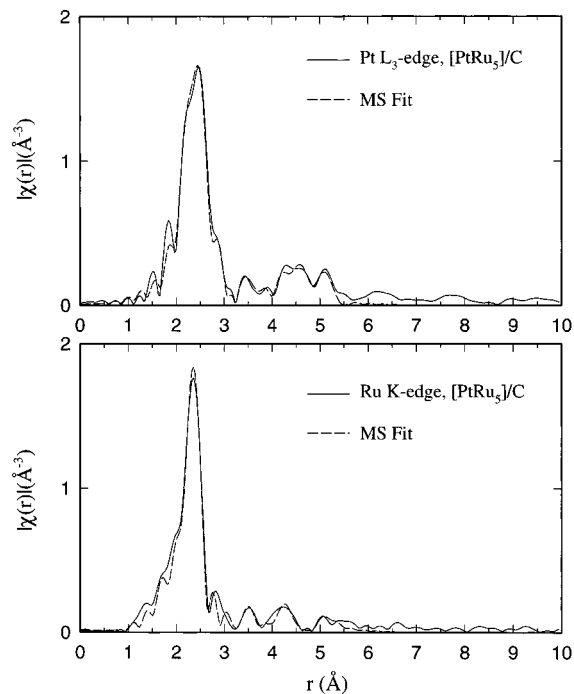


**Figure 10.** Fourier-transformed EXAFS data measured at 190 K from the carbon-supported  $[PtRu_5]/C$  nanoparticles after activation at 673 K under  $H_2$  (solid) and the multiple scattering fit results (dash): (a) Pt  $L_3$  and (b) Ru K edges.

**Table 1.** Metal Bond Distances Obtained by Simultaneously Fitting the Pt  $L_3$  and Ru K edge EXAFS Data Measured from the Carbon-Supported  $[PtRu_5]/C$  Nanoparticles

bond	bond distance (Å)			
	first shell	second shell	third shell	fourth shell
Pt–Pt	2.69(3)	3.78(3)	4.66(4)	5.38(3)
Pt–Ru	2.70(1)	3.79(2)	4.70(2)	5.40(1)
Ru–Pt	2.70(1)	3.79(2)	4.70(2)	5.40(1)
Ru–Ru	2.67(1)	3.78(1)	4.68(1)	5.42(2)

The Pt  $L_3$  and Ru K edge data measured from the nanoparticles were fit simultaneously using a two-step procedure. The advantage of simultaneous fit to the two edges of the same material is in decreasing the ratio between the number of fit variables and the number of independent points in the data. This is possible since the structural parameters of the heterometallic bonds (i.e., Pt–Ru and Ru–Pt) must be the same, as seen from each edge, while the number of independent points doubles when adding a new data set. Briefly, the first step required the simultaneous fitting of both edges in the  $r$  range 2.0–3.1 Å with the first-shell single scattering paths (i.e., Pt–Ru(1), Pt–Pt(1), Ru–Pt(1), and Ru–Ru(1)). Then, the first-shell results were fixed while the higher-shell data were fit in the  $r$  range 3.1–5.5 Å. We found that, when fitting the higher-shell EXAFS data, the DWFs for the paths and coordination numbers were strongly correlated, leading to large uncertainties in both values. Thus, the DWFs for the higher-shell scattering paths were constrained to be equal to the values found in the fit of the first shell of each of the respective bonding interactions. This assumption may result in the underestimation of the higher-shell coordination numbers because these shells typically possess larger DWFs than the corresponding first shells. The results of the first- and higher-shell fits are displayed in Tables 1 and 2 (see also Figure 10).

The first-shell bond distances determined from the fit (Table 1) are consistent with the values found in the reference materials. The higher-shell bond distances, which inherently carry a larger

**Table 2.** Metal Coordination Numbers Obtained by Simultaneously Fitting the Pt L<sub>3</sub> and Ru K edge EXAFS Data from the Carbon-Supported [PtRu<sub>5</sub>]/C Nanoparticles

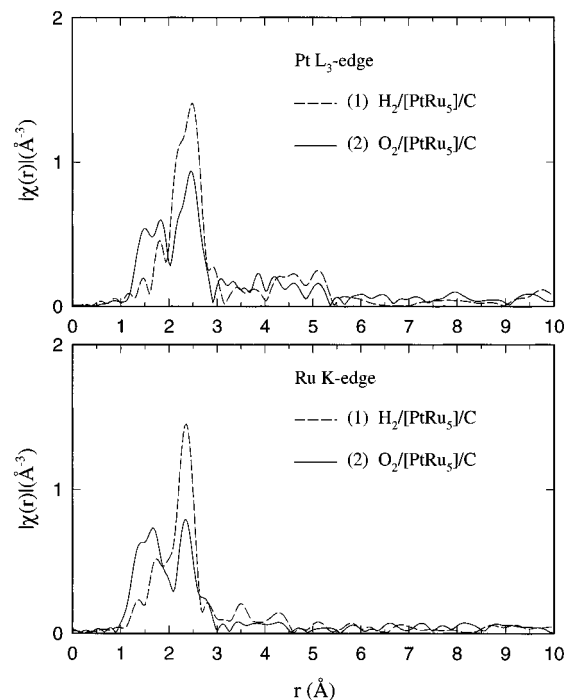
bond	coordination number			
	first shell <sup>a</sup>	second shell	third shell	fourth shell
Pt–Pt	2.5(1.6)	1.4(6)	1.9(1.4)	1.4(8)
Pt–Ru	4.0(1.0)	1.0(5)	3.0(1.0)	1.5(5)
Ru–Pt	0.7(2)	0.2(1)	0.6(2)	0.3(1)
Ru–Ru	5.4(5)	1.3(3)	2.8(4)	0.8(3)

<sup>a</sup> Debye–Waller factors (DWFs) determined for the first shells were as follows: Pt–Pt, 0.0041(32) Å<sup>2</sup>; Pt–Ru/Ru–Pt, 0.0028(15) Å<sup>2</sup>; Ru–Ru, 0.0044(5) Å<sup>2</sup>. The higher-shell data were constrained to have the same DWFs for the respective metal bonds.

uncertainty, are consistent (within the determined errors) with the extension of the first-shell data. In general, the fitting results for the first-shell coordination numbers (Table 2) reflect the Ru-rich nature of the precursor. The fact that significant Pt–Pt bonding is present demonstrates that the nanoparticles must be obtained from condensation of several molecules of the precursor PtRu<sub>5</sub>C(CO)<sub>16</sub>. The data also suggest that the structural environments sampled by the Pt and Ru centers in the supported particles are not statistical, and thus, some degree of atomic segregation must occur. Several lines of reasoning bear on this latter point, as discussed below.

The marked compositional asymmetry in the first-shell coordination environments of Pt and Ru determined by fitting (Table 2) shows a stronger weighting of the homometallic coordination. This can be quantified by comparing the statistically predicted ratio of Ru–Pt bonds to Ru–M bonds ( $N_{\text{RuPt}(1)}/N_{\text{RuM}(1)}$ ) with the value determined by EXAFS. The statistical distribution of metal neighbors around the Ru for the 1:5 composition would result in a  $N_{\text{RuPt}(1)}/N_{\text{RuM}(1)}$  ratio of 0.17, whereas the value found by EXAFS is  $0.12 \pm 0.03$ . Similarly, the statistical  $N_{\text{PtRu}(1)}/N_{\text{PtM}(1)}$  ratio is 0.83 and the value determined by EXAFS is only  $0.4 \pm 0.3$ . Both of these values clearly demonstrate preferential Pt–Pt and Ru–Ru bonding, at the expense of heterometallic bonding in the nanoparticles, i.e., a nonstatistical distribution of the two metals. As discussed below, similar results are found in an analysis of the higher-shell coordination numbers (Table 2). The most important finding to note is the presence of ordered shell structure at distances as high as 5 Å that can be fit quantitatively with the fcc structure.

**Chemisorption of Oxygen.** The introduction of a 1:1 mixture of O<sub>2</sub>:He (40 mL/min) into the catalyst cell at room temperature results in the oxidation of the nanoparticles as evidenced by the dramatic changes seen in the EXAFS data (Figure 11). The EXAFS data shows significant reduction in the amplitude for the first-shell metal–metal bonding ( $r$  range 2–3 Å) and the formation of metal–oxygen bonds in the  $r$  range 1–2 Å. Quantitative fitting results reveal that the changes in the first metal shell amplitude are due primarily to increases in the static disorder (i.e., DWFs) for these bonds after exposure to oxygen (Pt–Pt, 0.0141(66) Å<sup>2</sup>; Pt–Ru/Ru–Pt, 0.0087(52) Å<sup>2</sup>; Ru–Ru, 0.0101(19) Å<sup>2</sup>). It is not clear, given the uncertainties, if the metal coordination numbers have changed appreciably from the values found in the reduced nanoparticles. On the basis of fitting results of the oxygen shell (in the  $r$  range 1–2 Å),  $2.3 \pm 0.7$  Pt–O and  $1.8 \pm 0.6$  Ru–O bonds are formed with lengths of  $1.97 \pm 0.03$  and  $2.05 \pm 0.04$  Å, respectively. The oxidation is easily reversed by discontinuing the O<sub>2</sub>/He flow and re-exposing the sample to a H<sub>2</sub> atmosphere at room temperature. The EXAFS data measured after the reintroduction of H<sub>2</sub> revealed that the metallic structure of the particles is easily recovered (as shown in Figure 10); the fitting results suggest

**Figure 11.** Evolution of EXAFS associated with the Pt L<sub>3</sub> (top panel) and Ru K edge (bottom panel): (1) after activation at 673 K under H<sub>2</sub> (dash); (2) after exposure to a O<sub>2</sub>/He (1:1) mixture for 10 min at 293 K (solid).**Table 3.** Calculated Coordination Numbers for Two Model Hemispherical Nanoparticles Based on the Cubooctahedral Structure<sup>a</sup>

edge length	bond	coordination number			
		first shell	second shell	third shell	fourth shell
3	Pt–Pt	3.00	0	1.00	1.00
	Pt–Ru	3.00	2.50	6.00	3.00
	Ru–Pt	0.58	0.48	1.16	0.58
	Ru–Ru	6.58	1.94	6.00	2.52
4	Pt–Pt	3.38	1.50	2.63	1.50
	Pt–Ru	3.75	2.06	7.13	3.75
	Ru–Pt	0.79	0.43	1.50	0.79
	Ru–Ru	7.58	2.68	9.08	4.18

<sup>a</sup> The 37-atom model, with an edge length of 3, is shown in Scheme 1. The 92-atom model has a four-atom edge length. In each model, the Pt is assumed to segregate to surface sites while maintaining the maximum Pt–Pt coordination. The diameters of these models bracket the sizes of the observed particles (see Figure 2).

no significant changes in the particle structure from that present prior the addition of oxygen.

## Discussion

The dispersion and chemical reduction of the PtRu<sub>5</sub>C(CO)<sub>16</sub> molecular cluster precursor on carbon black resulted in the formation of bimetallic nanoparticles with an average diameter of ca. 1.5 nm and extremely narrow compositional distribution centered on the nominal (1:5) Pt to Ru composition of the precursor. In the following discussion, we propose that the microstructure of the average nanoparticle is best modeled as an fcc hemisphere (Scheme 1) where the Pt atoms (dark) segregate to the surface of the nanoparticle and away from the substrate, maximizing the number of Pt–Pt bonds. For comparison, the first- and higher-shell coordination numbers for two model nanoparticles are displayed in Table 3. In the following discussion, we will consider several independent analyses that support this type of nanostructure and demonstrate how the average metal coordination numbers and the narrow

compositional distribution allow such detailed structural modeling.

To independently confirm and provide additional insight into the average nanoparticle morphology, we also used the first-shell coordination numbers determined from the Pt and Ru EXAFS data which can be used to estimate the average size and composition of the supported nanoparticles. In bulk close-packed structures (both fcc and hcp), one expects a value of 12 for the first-shell coordination. The value measured in the present work (of  $6.3 \pm 1.0$ ), based on the weighted average of the Ru and Pt first-shell coordination numbers, is significantly lower than this anticipated coordination number. The reduction in the first-shell coordination numbers, from the bulk metal value of 12, is directly related to the finite size of the nanoparticles, since there exist an increasing fraction of surface (i.e., lower coordination) sites as its size decreases.<sup>41</sup> This is illustrated in Figure 2 (left axis), which correlates the average first-shell coordination numbers for all metal atoms in an fcc hemisphere of Ru/Pt atoms (with lattice parameter,  $a = 3.78 \text{ \AA}$ ) based on the cuboctahedral structure. As shown in the plot, the experimentally measured average metal first-shell coordination number of 6.3 is consistent, within the experimental error, with an average particle diameter of 1.2 nm. This is close to the 1.6 nm value inferred from the microscopy. At this level of analysis, EXAFS data cannot show how narrow the size distribution might be, but it is clearly consistent with the microscopy results. It is interesting to note that for the corresponding spherical structure, i.e., cuboctahedron, the average coordination of 6.3 would correspond to a diameter ( $< 10 \text{ \AA}$ ) that is significantly smaller than the average value measured by STEM.<sup>41a</sup>

Heterometallic bonding in all shells (i.e.,  $N_{\text{PtRu}}$  and  $N_{\text{RuPt}}$ ) is strongly evidenced by the EXAFS data and thus provides direct evidence for the formation of bimetallic nanoparticles. Perhaps more intriguing, though, was the EDX compositional analysis of discrete particles which, as shown in Figures 3 and 4, indicated that the nanoparticle composition was indistinguishable from that of the precursor (to within the narrow limits of the experimental error).

The microdiffraction patterns measured from [PtRu<sub>5</sub>]/C nanoparticles are best modeled when indexed to an fcc close-packed crystal structure. The higher-shell structure seen in the EXAFS, which was quantitatively fit to the fcc model, also supports such an interpretation. It is therefore extremely interesting to note that the bulk Pt:Ru binary phase diagram predicts that a 1–5 atom % alloy would form a substitutional solid solution with an hcp crystal structure.<sup>31</sup> These results thus serve to demonstrate how the structures of bulk alloy phases may be significantly different from those of nanometer-sized metal ensembles of comparable composition since the structures adopted by the latter are strongly dependent on the minimization of the surface energy. The importance of this latter principal has been argued by others as well. For example, high-resolution electron microscopy studies have shown that Ru nanoparticles supported on amorphous carbon can adopt a variety of habits including fcc, hcp, and body-centered cubic crystal structures.<sup>6a</sup> These structures were shown to vary under continuous influence of the 400 kV electron beam. The presence of Pt may also help to nucleate the crystal growth of the fcc structure, as has been shown of the Pt–Re system on oxide supports.<sup>5c</sup>

Having established the narrow size and compositional distributions of these nanoparticles, it is possible to use the relative

coordination numbers determined for the two metals by EXAFS to construct a more detailed model of the average nanoparticle microstructure. A key to this model is the average first-shell coordination environments which indicated that both Pt and Ru favored a nonstatistical homometallic bonding (Table 2) in the nanoparticles. This suggests that segregation of Pt and Ru to nonstatistically rich environments of each of the respective metals occurs in the nanoparticle samples. Because the composition and size distributions of the supported particles are narrow, the nonrandom distribution cannot arise from the segregation of Pt and Ru into discrete single element clusters. The differences observed in the average Pt and Ru coordination numbers must, therefore, reflect variations in the average intraparticle distribution of metals because the EXAFS data reflects an average environment in a nearly homogeneous (in size and composition) population of particles. Intraparticle segregation can only result from the partitioning of Pt toward the interior or the surface of the nanoparticle. Given the size of the average particle ( $\sim 1.5 \text{ nm}$ ), the small number of Pt atoms ( $\sim 6$ ) could easily reside in strictly interior sites resulting in a Pt first-shell metal coordination close to 12. The first-shell Pt–M(1) coordination ( $6.5 \pm 2.6$ ) does not support this model (Table 2). The Pt–M coordination number does support segregation to the surface, however.

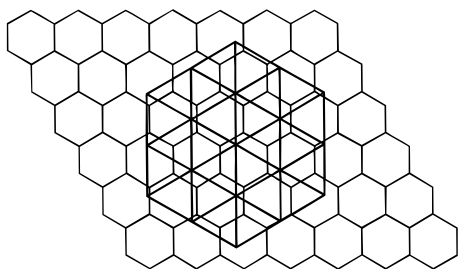
In the model nanoparticle, shown in Scheme 1, the surface segregated Pt atoms (dark) have an average first-shell coordination of six metal neighbors while the remaining Ru atoms have an average coordination of 7.2 (Table 3). The experimental first-shell coordination numbers (Table 2) are consistent with the small fraction of Pt segregating to only surface sites. Furthermore, the fraction of heterometallic bonding in the model nanoparticle around Pt and Ru is also consistent with the experimental data. The heterometallic Ru bond ratio in the model nanoparticle,  $N_{\text{RuPt}}^{(m)}/N_{\text{RuM}}^{(m)}$ , is 0.08, while the heterometallic Pt bond ratio,  $N_{\text{PtRu}}^{(m)}/N_{\text{PtM}}^{(m)}$ , is 0.50. The experimental data yields values of  $0.12 \pm 0.03$  and  $0.4 \pm 0.3$ , for the fraction of heterometallic bonds around Ru and Pt, respectively. Therefore, the large asymmetry in the first-shell coordination numbers measured from the [PtRu<sub>5</sub>]/C nanoparticles can be easily explained as a nonstatistical distribution of the two metals, where Pt preferentially segregates to surface sites, maximizing the number of Pt–Pt bonds. For similar calculations carried out on a model nanoparticle with a four-atom edge length, similar conclusions may be drawn.

The higher-shell coordination numbers found in the nanoparticles provide additional insight and verification of the proposed structural model. The higher-shell structure of the Pt EXAFS data, which is significantly more intense than the corresponding Ru data, must also be attributed to the nonrandom distribution of the respective absorbers. Fitting these shells using the FEFF6 multiple-scattering code provided a quantitative determination of these differences. Interestingly, fitting indicated that the difference between the two absorbers was the large fraction of higher-shell Pt–Pt bonding in the third and fourth shells of the Pt EXAFS (as also found in the first-shell analysis). On the other hand, the Ru–Ru contribution present in the Ru edge data has significantly lower coordination numbers (or higher DWFs) in these shells. These relative results are consistent with the first-shell data which suggested that the Pt segregates into Pt rich domains.

We note that the absolute M–Ru coordination numbers from the nanoparticles (Table 2) diverge from the structural model coordination numbers (Table 3) in the third and fourth shells. Insight may be gained into the actual structure of the nanoparticles by noting the differences between the nanoparticle data

(41) (a) Benfield, R. E. *J. Chem. Soc., Faraday Trans.* **1992**, *88*, 1107. (b) van Zon, J. B. A. D.; Koningsberger, D. C.; van't Blik, H. F. J.; Sayers, D. E. *J. Chem. Phys.* **1985**, *82*, 5742. (c) Gallezot, P.; Bienenstock, A. I.; Boudart, M. *Nouv. J. Chim.* **1978**, *2*, 263.

Chart 1



and the structural model used in the fit. We believe that these differences are related to the use of the first-shell DWFs in the analysis of the higher-shell structure. The first-shell values may be significantly lower than the actual higher-shell DWFs, resulting in an underestimation of the absolute higher-shell coordination numbers. Therefore, the large divergence in the Ru–M coordination numbers in the third and fourth shells, compared with the Pt–M coordination numbers, may reflect differences in the relative ordering of the Pt and Ru domains.

Differences in the ordering (DWFs) of the Pt and Ru domains may be related to the reducibility of the two metals. For example, Ru, which is more oxophilic than Pt, may form stronger bonds to the carbon black surface-functionalities (and possible impurities), resulting in a wider distribution of measured Ru–M bond distances. Additionally, carbon impurities from the carbide core of the parent compound may be present. These differences would be interpreted via EXAFS as disorder (i.e., a larger DWF) because they would result in small static variations ( $\pm 0.05$  Å) in the M–M bond distances. Although the specific bonding interactions with the support (or impurities) were neglected, due to the relatively low-signal level associated with these bonding contributions, they must be present in some measure because they provide a barrier to further condensation of the metals during reduction. One would expect, as illustrated by the simple geometric model shown in Chart 1, that an incommensurate structure is formed by the interaction of the hexagonal Ru lattice and the graphitic functionalities of the carbon black surface (since  $d_{\text{Ru–Ru}} = 2.67$  Å and  $d_{\text{C–C}} = 1.42$  Å).<sup>42,43</sup>

The model structure described above finds precedent in other studies of both Pt–Ru supported particles<sup>14a,44</sup> and bulk Pt–Ru alloys.<sup>23</sup> For example, in situ EXAFS was measured from Pt–Ru/C catalysts (E-TEK) under potential control in 1 M HClO<sub>4</sub> by McBreen et al.<sup>14a</sup> The nanoparticle compositional distribution in this formulation was large due to a large fraction of unalloyed Ru, however. A significant fraction of the more oxophilic Ru atoms may be stabilized as a nonreducible oxidic phase. The use of the PtRu<sub>5</sub>C(CO)<sub>16</sub> precursor has clearly eliminated this problem, allowing the formation of a very narrow compositional distribution of nanoparticles centered on the nominal precursor composition. It is interesting to note that we do observe differences in the reducibility of the two metals as a difference in the ordering of the Pt and Ru domains. In

(42) Dresselhaus, M. S.; Dresselhaus, G.; Eklund, P. C.; Saito, R.; Endo, M. In *Carbon Nanotubes—Preparation and Properties*; Ebbesen, T. W., Ed.; CRC: New York, 1997; Chapter 1.

(43) The structural model shown in Scheme 2 was based on the face capping bonding geometry of benzene (Johnson, B. F. G.; Lewis, J.; Matinelli, M.; Wright, A. H.; Braga, D.; Grepioni, F. *J. Chem. Soc., Chem. Commun.* **1990**, 364) and C<sub>60</sub> (Hsu, H.-F.; Shapley, J. R. *J. Am. Chem. Soc.* **1996**, *118*, 9192) with triangular Ru<sub>3</sub>(CO)<sub>9</sub> clusters. In both analogues, the Ru<sub>3</sub> triangle is centrally located over the C<sub>6</sub> ring with each Ru positioned over alternate C–C bonds of the benzene or the fullerene framework.

(44) (a) Miura, H.; Gonzalez, R. G. *J. Phys. Chem.* **1982**, *86*, 1577. (b) Alerasool, S.; Gonzalez, R. D. *J. Catal.* **1990**, *124*, 204. (c) Radmilovic, V.; Gasteiger, H. A.; Ross, P. N. *J. Catal.* **1995**, *154*, 98.

addition, segregation has been previously described by other investigators of bimetallic nanoparticles.<sup>5,6b–e,7,44a,b</sup> For example, Sinfelt et al. found significant nonrandom distributions in bimetallic systems and attributed it to the formation of raftlike structures in which there is a preferential surface segregation.<sup>5a</sup> The presence of Pt surface segregation also has precedent in bulk Pt<sub>x</sub>Ru<sub>1–x</sub> alloy phases. For example, Ross et al. found a >90% surface enrichment of Pt in bulk alloys with low Pt compositions ( $\sim 9$  atom %).<sup>23</sup>

**Chemisorption of Oxygen.** As evidenced by the evolution of the EXAFS data (Figure 11), the supported [PtRu<sub>5</sub>]/C nanoparticles react vigorously with O<sub>2</sub>. This reaction produces significant albeit reversible changes in the average microstructure of the nanoparticle. The increase in the disorder in the first-shell metal bond lengths is accompanied by the average bonding of ca. two oxygens to both Pt and Ru at bond distances that are similar to those found in structures with bridging oxygen atoms. In PtO, the Pt atoms are coordinated by four oxygen atoms in a tetrahedral arrangement with a bond length of 2.02 Å,<sup>45</sup> and in RuO<sub>2</sub>, the Ru is coordinated by six oxygens with a distorted octahedral structure with a bond length of 1.96 Å.<sup>46</sup> Both structures are composed of three-dimensional arrays of M–O–M linkages. It is clear that the average M–O coordination numbers in the oxidized nanoparticles are significantly lower than those found in the bulk oxides. The other significant difference from the bulk phases is the presence of metal–metal bonds (the shell seen at 2.7 Å, Figure 10) that are retained in the oxidized nanoparticle microstructure. The structural data, therefore, indicate that only a fraction of the particle experiences a perturbation in the bonding.

The qualitative structural features can be interpreted in the context of a simple model. In a 1.5 nm diameter hemispherical particle (Scheme 1), more than 50% of the atoms are present at the surface. The experimentally observed metal–oxygen bonds (with an average number of two oxygen bonds per metal) is consistent with the formation of an MO<sub>x</sub> surface layer with the core of the nanoparticle retaining its close-packed structure. The surface oxide layer (which passivates the particle and prevents further oxidation) is easily reduced (i.e., in minutes at 293 K under 1 atm of H<sub>2</sub>).

Similar models have been invoked to explain results obtained in previous investigations of the reactions of oxygen and hydrogen with supported Pt particles.<sup>47</sup> These studies generally indicate that the oxidation of the particle surface is facile; the structure of this oxide layer appears to depend strongly on the particle size, however. The available data are generally explained by assuming the formation of either a chemisorbed oxide layer or, under more pressing conditions, the formation of a compound oxide species.<sup>47b–d</sup> Subsequent ease of reduction by hydrogen was attributed to the presence of a (largely) unoxidized metal core, which promotes the dissociative chemisorption of hydrogen and consequent reduction of the particle under mild conditions.<sup>47</sup>

## Conclusions

Bimetallic nanoparticles supported on carbon black were prepared from a PtRu<sub>5</sub>C(CO)<sub>16</sub> molecular cluster precursor by

(45) (a) Moore, W. J.; Pauling, L. *J. Am. Chem. Soc.* **1941**, *63*, 1392. (b) Hecq, M.; Hecq, A. *J. Less Common Met.* **1977**, *56*, 133.

(46) Sorantin, P. I.; Schwarz, K. *Inorg. Chem.* **1992**, *31*, 567. (b) Baur, W. H. *Acta Crystallogr.* **1971**, *B27*, 2133.

(47) (a) Nandi, R. K.; Molinaro, F.; Tang, C.; Cohen, J. B.; Butt, J. B.; Burwell, R. L. *J. Catal.* **1982**, *78*, 289. (b) Huizinga, T.; van Grondelle, J.; Prins, R. *Appl. Catal.* **1984**, *10*, 199. (c) Park, S. H.; Tzou, M. S.; Sachtler, W. M. H. *Appl. Catal.* **1986**, *24*, 85. (d) McCabe, R. W.; Wong, C.; Woo, H. S. *J. Catal.* **1988**, *114*, 354. (e) Deutsch, S. E.; Miller, J. T.; Tomishige, K.; Iwasawa, Y.; Weber, W. A.; Gates, B. C. *J. Phys. Chem.* **1996**, *100*, 13408.

activation in H<sub>2</sub> at 673 K. The EXAFS data indicated that bimetallic nanoparticles were formed where the Pt centers segregate to the surface of the fcc Ru structure. Differences in the average coordination environments of the two metals reflect the preferential occupation of surface sites by the Pt centers. In support of the spectroscopic measurements, microscopy demonstrated the formation of an extremely narrow size distribution centered around an average diameter of ca. 1.5 nm. The compositional distribution, which was found to be centered on a 1:5 ratio of Pt to Ru, suggests a uniform coalescence of the precursor clusters upon activation. Microdiffraction measurements indicated the formation of nanoparticles with an fcc microstructure even though the bulk structure for this composition is hcp. The nanoparticles undergo reversible oxidation forming a surface composed of MO<sub>x</sub> and core of metal.

These results provide exciting precedent for the preparation of carbon-supported Pt–Ru nanoparticles with compositions that span the binary phase diagram. Further studies of the structure

and reactivity of these phases may provide insight into the nature of the compositional differences found in the activity toward methanol oxidation in DMFCs.

**Acknowledgment.** We are especially grateful to Richard Vanfleet for his insightful discussions and help devising suitable data sampling methods for the microdiffraction experiments and to Peggy Mochel for her technical assistance operating the STEM. We thank Kwangyeol Lee for preparing PtRu<sub>5</sub>C(CO)<sub>16</sub>. We also thank Professor Ian Robertson for metal powders and use of the arc-melter as well as Eric Hollar for his technical assistance. This work was funded by Office of Naval Research (N00014-96-1-0490) and the University of Illinois Frederick Seitz Materials Research Laboratory, which is supported by the Department of Energy (DEFG02-91-ER45439). M.S.N. acknowledges financial support via a fellowship award from the Department of Chemistry.

JA971039F